 doi:10.20944/preprints202203.0335.v1

Article

Method of formulating 3D-printable strain-hardening geopolymer composites for additive construction

Shin Hau Bong[1], Behzad Nematollahi[1,2*], Venkatesh Naidu Nerella[3] and Viktor Mechtcherine[3]

[1] Centre for Smart Infrastructure and Digital Construction, School of Engineering, Swinburne University of Technology, Australia
[2] Department of Civil and Structural Engineering, The University of Sheffield, Sheffield, UK
[3] Institute of Construction Materials, Technische Universität Dresden, Dresden, Germany
*Corresponding author: bnematollahi@swin.edu.au

Abstract: One of the major limitations of the current 3D-concrete-printing technology is incorporation of reinforcement. Furthermore, there is a need to decrease the ecological footprint of printable concrete. As a possible solution for these challenges, this paper presents a 3D-printable strain-hardening geopolymer composite (3DP-SHGC) that shows pseudo-ductile behaviour under direct tension. The developed 3DP-SHGC is composed of one-part (just-add-water) geopolymer binder made of slag (GGBFS), fly ash (FA) and solid activator. The one-part geopolymer binder eliminates the need for elevated temperature curing and handling of corrosive alkaline liquids. At first, an optimum matrix was identified by studying the effects of FA to GGBFS ratio on the rheological properties and compressive strength. Subsequently the optimum matrix was reinforced by PVA fibres to make the 3DP-SHGC, which printing performance and rheological properties were evaluated. In addition, the influences of curing temperature on the compressive, flexural and tensile performances of the printed specimens were also investigated. The results were compared with those obtained for the mould-cast specimens. The 3DP-SHGC exhibited superior flexural performance, higher tensile strength, and comparable tensile strain capacity to the mould-cast counterpart. Further, the curing temperature had influence on the mechanical properties of both 3D-printed and mould-cast SHGCs. The underlying reasons for the differences are discussed.

Keywords: 3D-concrete-printing; strain-hardening geopolymer composite; rheological properties; mechanical properties; strain-hardening

1. Introduction

The construction-related industries are considered as the largest industries in the world economy as the construction-related spending was reported to be about 13% of the global GDP in 2016 [1]. However, the industry has shown significantly lower productivity as compared to other manufacturing industries such as automotive and aerospace industries [1], and nearly no increase in productivity over the last decades. Compared to other industries which have adopted automation in their manufacturing process, the construction industry has relied primarily on manual labour. In addition, the construction industry has also been suffering from a high accident rate and high construction cost [2]. To tackle these issues, the construction industry is moving towards implementation of digital and automation technologies in recent years. Three-dimensional concrete-printing (3DCP) is one of the digital technologies that eliminates the use of expensive formwork for manufacture of concrete members with intricate geometries via an additive manufacturing process. However, there are many challenges still needed to be overcome before 3DCP can be routinely implemented into a practical construction scale [3, 4].

Incorporating conventional steel reinforcement in the extrusion-based 3DCP process is one of the primary challenges, which still needs to be addressed [5]. Over the past few years, few reinforcement solutions have been proposed to enhance the flexure and tensile performances of printed concrete members, such as post-installed steel reinforcement [6,

 doi:10.20944/preprints202203.0335.v1

7], vertical mesh reinforcement [8], continuous cable reinforcement [9, 10], carbon yarn reinforcement [11] and short-fibre reinforcement [12-14]. Among the aforementioned reinforcement methods, short-fibre reinforcement is currently one of the most promising, easy-to-implement reinforcement methods for the extrusion-based 3DCP processes; see e.g. [15]. Here, short-fibres can be blended into the fresh mixture directly during the mixing process to enhance the tensile and/or flexural performances of the printed concrete members without the need of special-designed extruder or any further extra process for reinforcement integration.

Strain-hardening cementitious composites (SHCC), also referred to as engineered cementitious composite (ECC), is an advanced fibre-reinforced cementitious composites exhibiting quasi-ductile behaviour accompanied by multiple fine cracks. Multiple cracking is absolutely essential for such material parameters as fracture toughness, work-to-fracture or strain capacity [16-18]. SHCC can be a part of the solution for reducing or eliminating the necessity for steel reinforcements in the printed concrete members [19]. Few studies have been carried out on developing 3D-printable SHCC [20-25]. For instance, Soltan and Li [21] developed a 3D printable SHCC mixture by investigating the influences of several additives on the printing performances (extrudability and buildability) of fresh SHCC mixtures. The 3D-printed SHCC specimens with optimum additives exhibited ultimate tensile strength of about 6.0 MPa and tensile strain capacity of about 4.0%. Ogura et al. [20] formulated 3D-printable SHCC with HDPE fibres, which exhibited remarkable strain-hardening behaviour under direct tensile loading. They also reported that, these behaviours were superior to those of mould-cast specimens [20]. Zhu et al. [22] investigated the influences of fibre content (1.0 vol.%, 1.5 vol.% and 2.0 vol.%) on the properties of printable SHCC mixtures. They succeeded to develop 3D-printable SHCC mixtures, which exhibited ultimate tensile strength and tensile strain capacity of up to 5.7 MPa and 11.4%, respectively. Ye et al. [24, 25] investigated the effects of crumb rubber content and fibre content in 3D-printable SHCC mixtures. The SHCC mixture with 40% (by volume fraction of silica sand) crumb rubber and 1.5 vol.% of polyethylene fibre was determined as the optimum mix for 3D printing, showing ultimate tensile strength and tensile strain capacity of 5.8 MPa and 7.5%, respectively. A comprehensive overview on printable SHCC/ECC can be found in [15].

It needs to be emphasised that all the 3D-printable SHCCs developed above are using ordinary Portland cement (OPC) as the main binder in their mixture compositions. The high embodied energy and carbon emissions because of the OPC production can compromise the sustainability performance of 3DCP with SHCC [26, 27]. Developing a 3D-printable strain-hardening geopolymer composites (3DP-SHGC), in which OPC is 'completely' replaced by geopolymer, can help to master this sustainability challenge, while still providing the necessary mechanical characteristics. In this article, a systematic approach of developing a 3DP-SHGC for the extrusion-based additive manufacturing is presented. The influence of mass ratio of fly ash (FA) to ground granulated blast furnace slag (GGBFS) on the rheological properties and compressive strength of the resulting geopolymer matrices were studied. Furthermore, the influence of curing temperature on the compressive strength of the resulting geopolymer matrices was also investigated. The matrix with desirable rheological properties and mechanical strength was then selected to be used for the 3DP-SHGC. The developed 3DP-SHGC should exhibit strain- and, subsequently, also deflection-hardening behaviours under direct tension and bending, respectively, while providing adequate printing performance for large-scale 3DCP process. Hence, the printing performance characteristics, including extrudability and buildability, rheological properties of fresh material and mechanical properties of the hardened 3DP-SHGC are evaluated in this paper. Furthermore, the influence of curing temperature on the mechanical properties of the developed 3DP-SHGC was also evaluated and compared with those of the conventionally mould-cast counterpart.

2. Materials

 doi:10.20944/preprints202203.0335.v1

The geopolymer source materials were Class F FA and GGBFS, the chemical composition of which are presented in Table 1.

Table 1. Chemical composition of the slag and fly ash (wt.%).

Chemical	Slag	Fly ash
Al_2O_3	12.53	24.89
SiO_2	32.19	56.74
CaO	43.23	5.20
Fe_2O_3	0.43	6.87
K_2O	0.29	0.885
MgO	5.69	1.35
Na_2O	0.26	0.42
P_2O_5	0.03	0.618
TiO_2	0.60	1.42
MnO	0.16	0.08
SO_3	4.02	0.266
L.O.I.[a]	0.39	1.22

[a] Loss on ignition.

The D50 and D10 values of the fine silica sand used for the production of SHGC were 176 μm and 108 μm, respectively. Anhydrous sodium metasilicate powder with alkali modulus of 0.9 (where alkali modulus = SiO_2/Na_2O mass ratio) and GD Grade sodium silicate powder with alkali modulus of 2.0 were used as the solid activators. Sucrose powder and nano clay were served as a retarder and viscosity modifying admixture in this study, respectively. The properties of the oil coated PVA fibre supplied by Kuraray Co. Ltd., Japan are given in Table 2.

Table 2. Properties of the PVA fibre.

Fibre type	Diameter (μm)	Length (mm)	Young's modulus (GPa)	Elongation (%)	Density (g/cm^3)	Nominal strength (MPa)
RECS 15	40	8	41	6	1.3	1600

3. Experimental Program

In this paper, the experimental program was performed in two stages as described below.

Stage I: Three geopolymer matrices were designed to investigate the influence of mass ratio of FA to GGBFS on the plastic viscosity, dynamic yield stress, static yield stress evolution and structural recovery of the resulting geopolymer matrices in fresh state as well as their compressive strength. In addition, the influence of curing temperature on the compressive strength was also investigated. The conventionally mould-cast specimens were used here to assess the compressive strength. Based on the results obtained, a matrix with desired rheological and mechanical properties was selected to be used as the matrix of the 3DP-SHGC in Stage II.

Stage II: The optimum matrix developed in Stage I was used for manufacturing the 3DP-SHGC, the properties in fresh and hardened states of which were then evaluated. In

 doi:10.20944/preprints202203.0335.v1

terms of the fresh properties, extrudability, buildability, plastic viscosity, dynamic yield stress, static yield stress evolution and structural recovery of the composite were evaluated. The effect of curing temperature on the hardened properties of the printed composite was also studied. Furthermore, the compressive strength of the printed composite was evaluated in different directions as related to direction of printing. The flexural performance of the printed composite was assessed by four-point bending test, while the tensile behaviour was assessed by conducting uniaxial tension test. The mould-cast SHGC specimens were also prepared and tested.

3.1. Mixture proportions and mixing procedures in Stage I

The mixture proportions of the one-part geopolymer matrices investigated in this stage are presented in Table 3. As shown in the table, the slag was partially (25%, 50% and 75% by mass) replaced by fly ash. The mass ratio of GD Grade sodium silicate powder to anhydrous sodium metasilicate powder was equal to 1.0 in all matrices. Sucrose powder (0.5% by mass of precursors) was used to longer the setting time of the matrices. Previous studies [28, 29] showed that the workability of geopolymer mixture can be significantly affected by the fly ash to slag mass ratio. To ensure all mixtures have adequate flowability for achieving good fibre dispersion while exhibiting good shape-retention-ability and buildability in Stage II of the investigation, the content of water of the matrices was adjusted so that they all exhibited comparable workability (i.e., approximately 200 mm average spread diameter after 25 strokes on the flow table as per the ASTM C1437 [30]).

To make the one-part geopolymer matrix, all dry ingredients were mixed in a mixer at low speed for 3 min. The water was then added, and the mixing was continued at low speed for 4 min. Subsequently, the mixing was continued at high speed for another 6 min to attain a high degree of homogenisation.

Table 3. Mixture proportions of one-part geopolymer matrices.

Mix ID	Fly ash	Slag	Activator[a]	Sand	Retarder[b]	Water
FA25	0.25	0.75	0.1	0.1	0.005	0.428
FA50	0.50	0.50	0.1	0.1	0.005	0.367
FA75	0.75	0.25	0.1	0.1	0.005	0.319

Note: All numbers are mass ratios of the precursor weight (fly ash + slag).

[a] Composed of 50% anhydrous sodium metasilicate and 50% GD Grade sodium silicate powders.

[b] Sucrose powder.

3.2. Mixing procedure in Stage II

The optimum matrix obtained in Stage I was used for manufacturing the 3DP-SHGC in Stage II. It should be noted that nano clay (0.2% by mass of precursors) was added to increase the cohesiveness of the matrix for better fibre dispersion [31], as well as enhancing the thixotropy property of the composite [32]. To make the 3DP-SHGC mixture, all dry ingredients including FA, GGBFS, solid activators, sand, sucrose powder and nano clay were dry mixed in a mixer for 3 min. The water was then slowly added, and the mixing was continued at low speed for 4 min. Subsequently, the PVA fibres with 2.0% by volume of the mixture were gradually added to the mixer and mixed at low speed for 3 min. Finally, the mixing was continued at high speed for another 3 min to guarantee uniform fibre dispersion.

3.3. Curing and testing of geopolymer matrices in Stage I

The influence of mass ratio of FA to GGBFS on the rheological behaviours of fresh one-part geopolymer matrix was investigated by using Viskomat XL rheometer by

Preprints (www.preprints.org) | NOT PEER-REVIEWED | Posted: 25 March 2022 doi:10.20944/preprints202203.0335.v1

Schleibinger (Germany); see [33] for technical details of the device. A six-blade vane probe (the diameter and height of the blades = 69 mm) was used in this study.

The evolution of static yield stress of the mixture was measured by conducting constant shear rate test at the resting times of 1 min, 5 min, 10 min and 15 min. Nerella et al. [34] addressed the single and multi-batch testing of static yield stress and substantiated single batch as a suitable method for testing materials for 3D printing. Subsequently, Ivanova et al. [35] showed that the difference between the results obtained from single- and multi-batch methods was insignificant. However, static yield stress determined at resting time of more than 15 min for 3D-printable one-part geopolymer mixture by sing-batch method showed significantly different result compared to that measured by multi-batch method [36]. Therefore, the static yield stress evolution of the geopolymer matrices was measured for up to resting time of 15 min by using single-batch method in this study. Considering the time required to transfer the fresh mixture from mixer to rheometer, all rheological measurements performed in this study were started at 3 min after end of the mixing procedure. In addition, an initial fixed shear rate test was performed at resting time of 1 second after the vane probe was inserted into the fresh mixture. This is to ensure the vane probe was positioned correctly before performing the first actual measurement (i.e., at the resting times of 1 min) [35]. A fixed low rotational velocity of 0.6 rpm was applied to the fresh mixture for 4 s at each resting time. Subsequently, the highest torque value recorded in each measurement was converted into static yield stress by using the Cauchy stress principle [37].

The hysteresis tests were performed to investigate the dynamic yield stress and plastic viscosity, the detailed procedure for which can be found in [38]. The protocol used for the hysteresis test is shown in Figure 1a.

The structural recovery behaviour (also called thixotropy property) of the optimum mixture and the control mixture were measured based on the method proposed by Li et al. [39], the rheological testing protocol for which is shown in Figure 1b.

The effects of curing temperature on the compressive strength of all matrices was also investigated. 50 mm cubic specimens were cast from each matrix. The mould-cast specimens were separated into two sets for curing at different temperatures. The first set was cured inside an oven at 60°C for 24 hours; however, the second set was cured for 28 days at room temperature (23 ± 3 °C). For each matrix, three mould-cast cubic specimens were made for each curing temperature. A loading rate of 20 MPa/min was used for compression testing of all specimens.

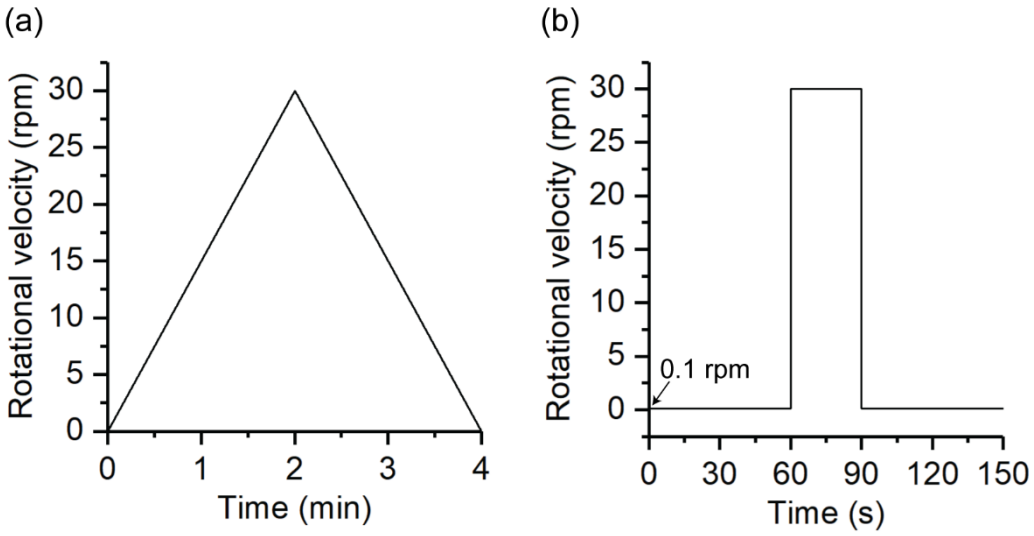

Figure 1. Rheological testing protocols for (a) hysteresis test and (b) structural recovery test. Reproduced from [38].

Preprints (www.preprints.org) | NOT PEER-REVIEWED | Posted: 25 March 2022 doi:10.20944/preprints202203.0335.v1

3.4. Printing process, curing and testing of 3D-printed SHGC in Stage II

A gantry-type 3DCP machine was used in printing the solid slabs and blocks for mechanical tests. A round nozzle with a 20 mm diameter was connected to the auger-type extruder. The printing speed and extrusion rate were 35 mm/s and ~0.75 L/min, respectively. For the compression tests the 5-layer slab measuring 400 mm × 380 mm × 50 mm (L × W × H) was printed. The 12-layer block measuring of 400 mm × 80 mm × 120 mm (L × W × H) was printed for the flexural and tensile tests. Each printed layer had a height of 10 mm. Similar to the curing regimes adopted in Stage I, the printed samples were separated into two sets for curing at different temperatures. After printing, the first set was sealed in a container and cured inside an oven at 60 °C for 24 hours. The second set was covered with a plastic sheet and left in the laboratory at ambient temperature (23 ± 3℃) for 28 days. The tests performed in Stage II are described below.

3.4.1. Extrudability and buildability assessment

The extrudability of fresh 3DP-SHGC mixture was assessed by printing a five-layer slab (L=400 mm × W=380 mm × H=50 mm) as schematically illustrated in Figure 2. Each printed layer has a length of almost 7.2 m; see the foregoing paragraph for details. The material was classified to have 'adequate' extrudability if the slab presented in Figure 2 could be printed successfully with no tearing of the printed filaments or any blocking in the extruder or delivery system.

The buildability of fresh 3DP-SHGC mixture was investigated by printing a column, the cross section of which was 200 mm × 300 mm as schematically illustrated in Figure 3. The column composed of 60 layers and the height of each layer was 10 mm. A 20 mm circular nozzle was used as in all other tests. The extrusion rate was ~0.45 L/min, while the printing speed was 20 mm/s.

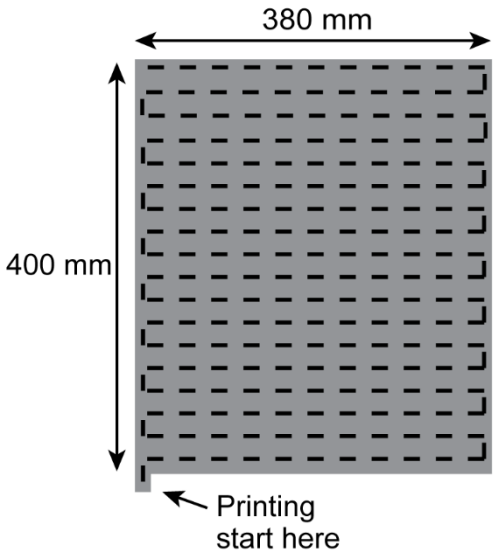

Figure 2. Schematic illustration of the slab for extrudability test; dotted line represents moving path of the extruder.

 doi:10.20944/preprints202203.0335.v1

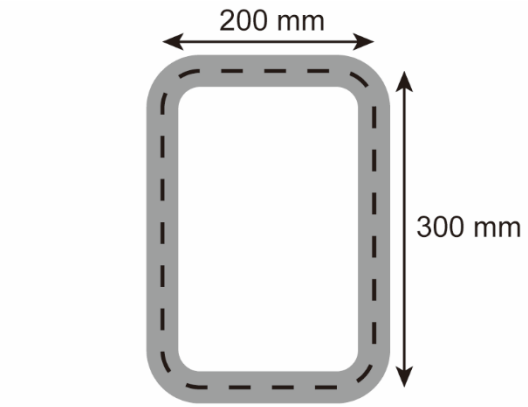

Figure 3. Dimensions of printed column for buildability test; dotted line represents moving path of the extruder. Reproduced from [38].

3.4.2. Rheological properties

The workability of fresh SHGC mixture was measured according to ASTM C1437 [30]. The static and dynamic yield stresses, plastic viscosity and structural recovery of fresh SHGC were measured in accordance with the testing procedures described in Section 3.3 by using the Viskomat XL rheometer.

3.4.3. Mechanical properties

To determine the compressive strength of the 3D-printed specimens, 50 mm cubes were sawn from the 5-layer printed slab. For comparison, conventional mould-cast 50 mm cubes with the same curing temperature were also made. The printed cubes were tested in compression in longitudinal, lateral and perpendicular directions as shown in Figure 4a. In each direction at least five specimens were tested in uniaxial compression at the rate of 20 MPa/min.

The flexural performance of the 3D-printed SHGC was investigated by performing four-point bending tests on beams sawn from the 12-layer printed blocks measuring L=350 mm × W=60 mm × H=20 mm. For comparison, conventionally mould-cast beams with the same dimensions and curing temperature were also manufactured. The printed beams were tested in perpendicular direction, see Figure 4b, with the mid-span of 100 mm and the rate of 0.5 mm/min. Four specimens were tested for each manufacturing process (i.e., 3D-printing or casting) and curing temperature.

Preprints (www.preprints.org) | NOT PEER-REVIEWED | Posted: 25 March 2022 doi:10.20944/preprints202203.0335.v1

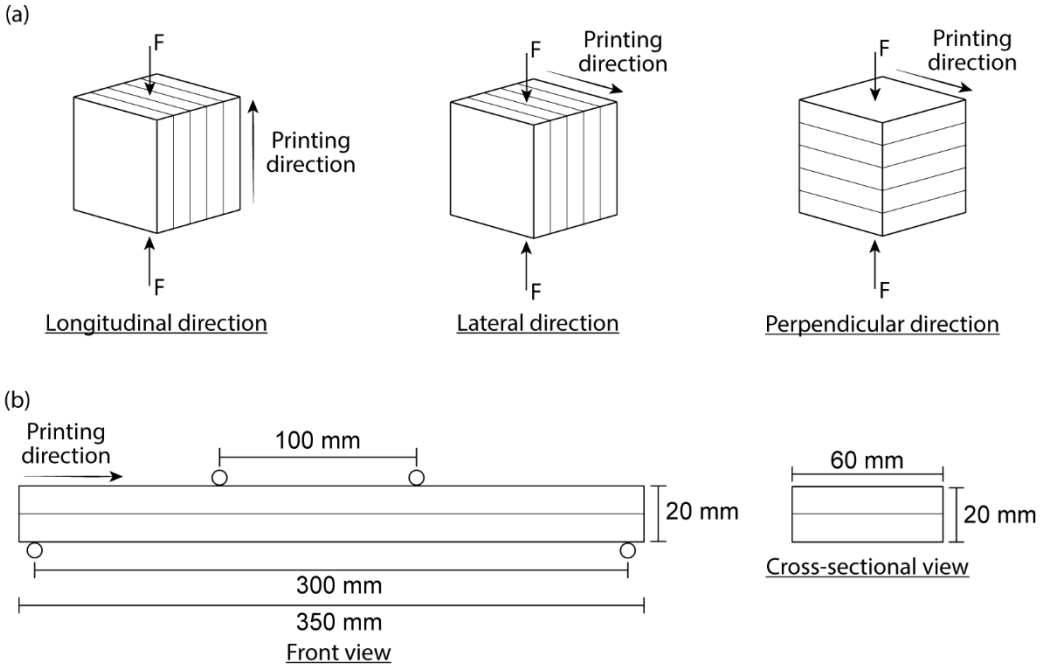

Figure 4. Testing directions for (a) compression and (b) flexural tests of 3D printed SHGC specimens.

To evaluate the tensile performance of the printed specimens, prismatic specimens measuring L=330 mm × W=30 mm × H=20 mm were saw-cut from the 12-layer printed blocks and placed in the dumbbell-shaped mould; see Figure 5a. Subsequently, the remaining empty spaces in the grip areas were cast with the same material to obtain dog dumbbell-shaped specimen; see Figure 5b. All printed specimens were tested at the earliest after 14 days of the mould-cast portions were cast to ensure adequate bonding between the printed specimen and mould-cast portions. A similar method has been utilised by Ye et al. [24, 25] to fabricate similar specimens for their 3D-printable ultra-high ductile concrete. For comparison, conventionally mould-cast dumbbell specimens with the same dimensions and curing temperature were also made. The uniaxial tension test setup is shown in Figure 6. A video extensometer was used to record the elongation in the gauge area. The printed specimens were measured in printing direction (i.e., longitudinal direction) at 0.5 mm/min. Three specimens were measured for each manufacturing process and curing temperature.

Preprints (www.preprints.org) | NOT PEER-REVIEWED | Posted: 25 March 2022 doi:10.20944/preprints202203.0335.v1

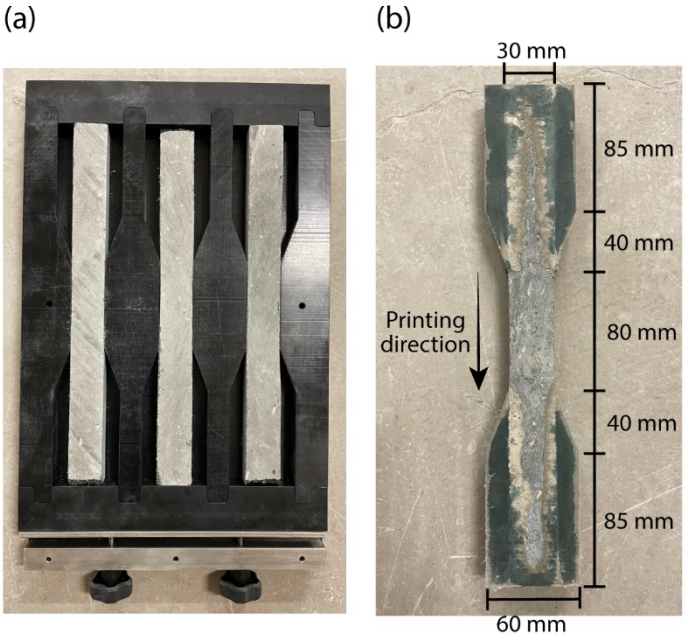

Figure 5. (a) Making dumbbell-shaped specimen from 3D-printed SHGC specimens and (b) dimensions of dumbbell-specimens.

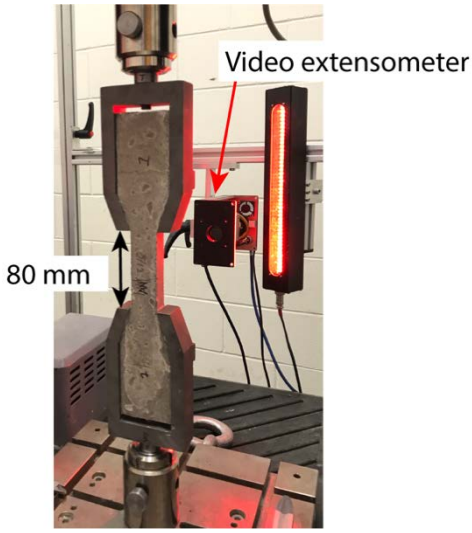

Figure 6. Uniaxial tension test setup.

3.4.4. Micromorphology characterisation

The micromorphology characteristics of facture surfaces was analysed using scanning electron microscopy (SEM, ZEISS® Supra 40 VP). The specimens were pre-coated with a thin conductive layer of gold. An accelerating voltage of 4 kV was used with working distance ranging between 11-15 mm.

4. Results and Discussions

4.1. Results of the Experimental Program in Stage I

4.1.1. Rheological properties

Figure 7 presents the evolution of static yield stress of all geopolymer matrices under investigation. FA75 exhibited the highest static yield stress among the matrices at each resting time, which is desirable to ensure high buildability and shape-retention-ability;

Preprints (www.preprints.org) | NOT PEER-REVIEWED | Posted: 25 March 2022 doi:10.20944/preprints202203.0335.v1

while FA25 has the lowest static yield stress at each resting time, which suggests that this mixture has the lowest buildability and shape-retention-ability [40-42]. The evolution of static yield stress of geopolymer mixture can be affected by both physical and chemical causes. As shown in Table 3, to achieve comparable workability for all matrices, the water content was reduced to compensate the increase of flowability due to increase of the content of spherical FA particles in the mixture. Several researchers have also reported that the flowability/workability increased when increasing the FA replacement in the FA-GGBFS blended geopolymers [29, 43, 44]. As a result, FA75 had the lowest water content among all the mixtures and consequently also less free water in the mixture. The low free water content in the mixture results in higher inter-particle friction, and thus higher stress is required to overcome the inter-particle friction and initiate the flow [45]. In addition, as the activator content is constant in all mixtures, the low water content in FA75 mixture leads to the higher viscosity of alkaline activator solution formed in the mixture, which could also increase the stress required to initiate the flow of the mixture. In the chemical sense, low water content in FA75 mixture also results in higher alkalinity of the mixture, which can promote the geopolymerisation reactions and greatly increase the static yield stress of the mixture over time [46].

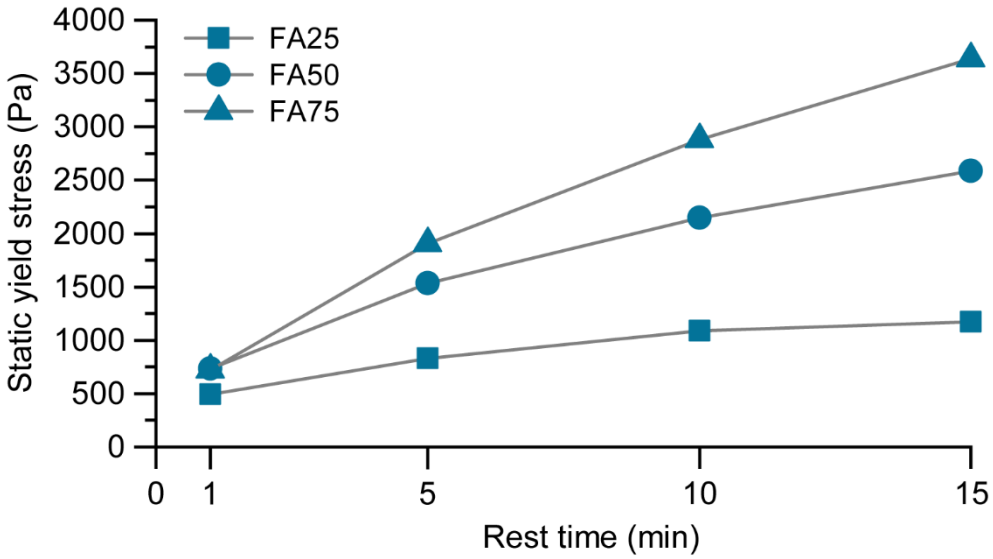

Figure 7. Static yield stress evolution of geopolymer matrices.

Figure 8 presents the descending curve measured in the hysteresis test for all geopolymer matrices under investigation. It should be pointed out that for each matrix a linear fitting line was drawn on the data obtained between 5 rpm to 30 rpm as these data were comparatively stable. Table 4 summarises the dynamic yield stress and plastic viscosity for all geopolymer matrices. According to Weng et al. [47], plastic viscosity and dynamic yield stress are closely related to pumpability of fresh printable mixture. As can be seen in Table 4, FA25 had the lowest dynamic yield stress and plastic viscosity among all the matrices, which is beneficial to ensure low pumping pressure during pumping or printing process. On the contrary, FA75 has the highest plastic viscosity and thus apparently least pumpability among all the matrices. Low water content in FA75 results in higher internal friction between particles and more viscous alkaline activator solution formed in the mixture, which increases the stress required to sustain the flow of the mixture.

Preprints (www.preprints.org) | NOT PEER-REVIEWED | Posted: 25 March 2022 doi:10.20944/preprints202203.0335.v1

Table 4. Dynamic yield stress and plastic viscosity of geopolymer matrices.

Mix ID	Dynamic yield stress (Pa)	Plastic viscosity (Pa.s)
FA25	42.9	8.6
FA50	74.2	16.7
FA75	62.0	26.8

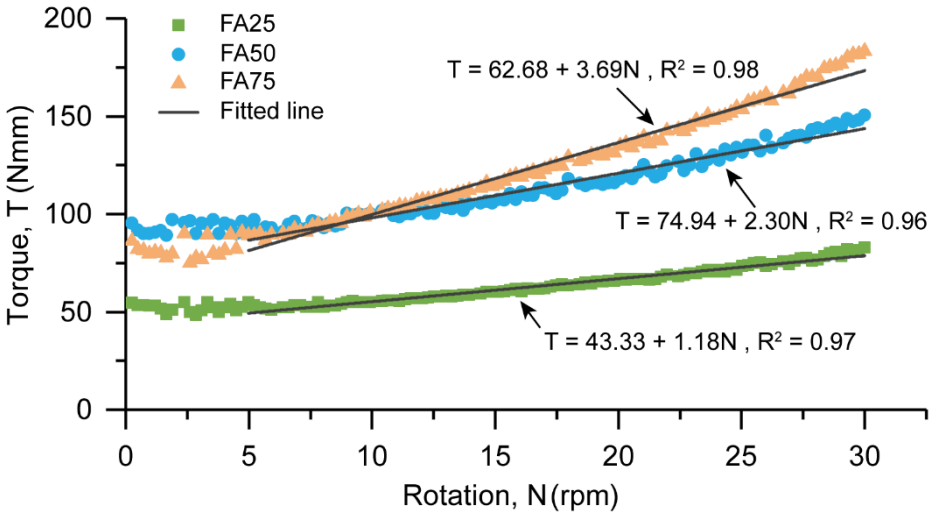

Figure 8. Descending curve of all geopolymer matrices measured in hysteresis test.

Figure 9 presents the apparent viscosity recovery results of all geopolymer matrices investigated in this part. As can be seen in the figure, FA75 exhibited the highest apparent viscosity at each stage followed by FA50 and FA25. As the apparent viscosity is the ratio of the measured shear stress to the applied shear rate, this result indicates that FA75 requires higher stress to shear as compared to FA50 and FA25 under the same applied shear rate, which is consistent with the plastic viscosity measurement showed in Table 4. As shown in the figure, all the matrices were able to restore most of their initial apparent viscosity after 60 s from Stage II. This showed that they all exhibited excellent thixotropic recovery, which enables the mixture to keep its shape after extrusion and rapidly gain strength to sustain upper layers without having any considerable deformation. Comparing all matrices under investigation, FA25 yielded the lowest recovery rate of 89% followed by FA75 (93%) and FA50 (94%). Since the difference in the recovery rates was relatively small, it can be said that all geopolymer matrices exhibited comparable thixotropic recovery, between 89% and 94%.

Preprints (www.preprints.org) | NOT PEER-REVIEWED | Posted: 25 March 2022 doi:10.20944/preprints202203.0335.v1

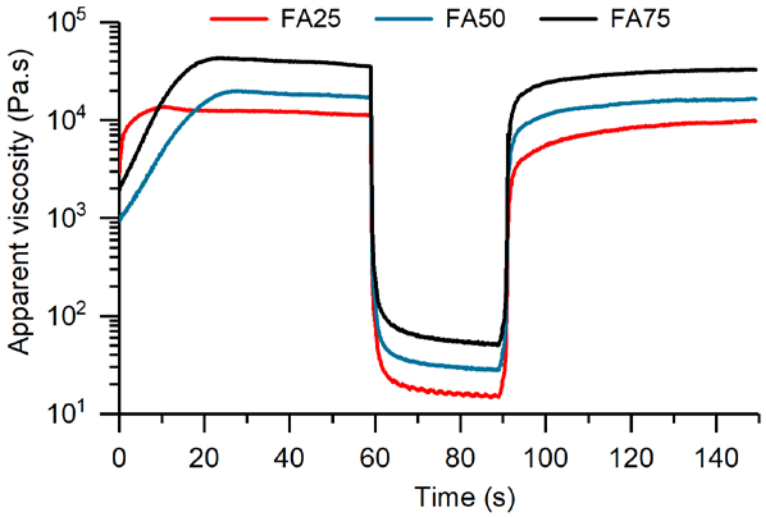

Figure 9. Apparent viscosity recovery of geopolymer matrices.

4.1.2. Mechanical strength

Figure 10 shows the compressive strength results for all geopolymer matrices depending on the curing temperature. FA75 exhibited the lowest strength among all the matrices regardless of the curing temperature, despite it had the lowest water content. Tennakoon et al. [44] reported a significant reduction in compressive strength of one-part FA-GGBFS blended geopolymer when the FA displacement was increased from 70% to 90% (by mass) of the total precursors. Ismail et al. [48] reported the mixture containing 75% or more FA did not set and hardened at 8 wt.% of activator dosage. The low strength values obtained in this study for FA75 indicate that the geopolymerisation reactions occurred in this composition were much less intensive as compared to that in FA25 and FA50, which led to a much weaker geopolymeric matrix. Furthermore, the compressive strength of heat cured specimens was lower than that of ambient cured samples even after 28 days. This was especially pronounced for FA75 composition, which yielded very low strength values in the case of heat curing. Further studies are required to investigate this phenomenon.

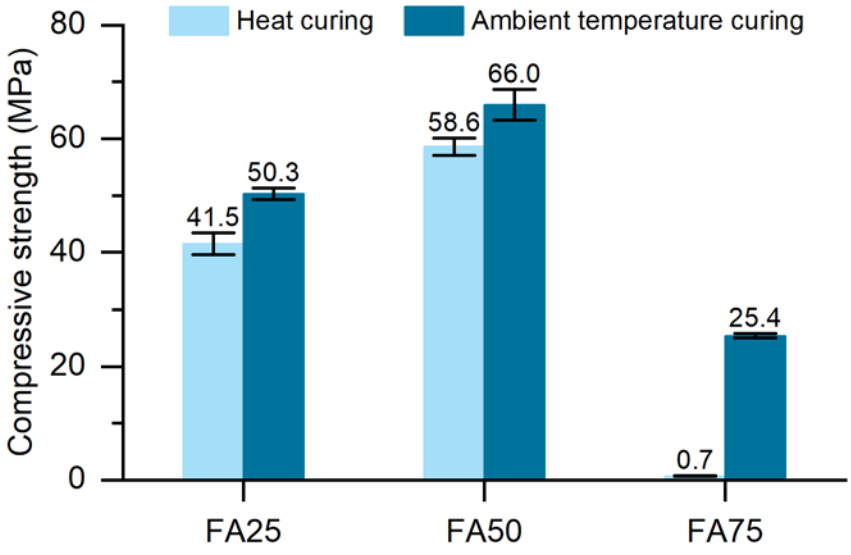

Figure 10. Compressive strength of geopolymer matrices.

FA50 showed the highest compressive strength, with values 31% to 41% higher than those obtained for FA25, depending on the curing temperature. Although FA25 apparently has better pumpability (i.e., lower dynamic yield stress and plastic viscosity)

 doi:10.20944/preprints202203.0335.v1

than FA50, the static yield stress evolution and apparent viscosity recovery rate of FA50 were higher than those of FA25, which is beneficial for FA50 to achieve better buildability and shape-retention-ability than FA25. In addition, the higher plastic viscosity of FA50 is particularly essential to ensure uniform fibre dispersion for achieving better deflection- and stain-hardening behaviours under bending and direct tension, respectively [49]. Hence, among the matrices studied in Stage I, FA50 was selected as the optimum matrix (balancing between FA25 and FA75) due to its desirable rheological properties and high strength.

4.2. Results of the Experimental Program in Stage II

4.2.1. Extrudability and buildability

Figure 11 shows the solid slab printed for extrudability evaluation. This 5-layer solid slab, where the total length of five layers was 36 m, was printed successfully without observing any blocking issue or tearing of the layers. Therefore, it can be concluded that the 3DP-SHGC developed in this study exhibited adequate extrudability.

Figure 12 shows the column printed using the 3DP-SHGC to assess its buildability. All 60 layers were extruded successfully without observing considerable deformation at the bottom layers. Hence, it can be said that the 3DP-SHGC showed adequate buildability. It is interesting to point out that the extruded SHGC filaments showed in Figure 11b and Figure 12 appeared to have wavy edges in contrast to the filaments with a smooth round edge showed in literature; see e.g. [50, 51]. This phenomenon seems to be a common issue when printing fibre-reinforced composite through a round nozzle [22, 52].

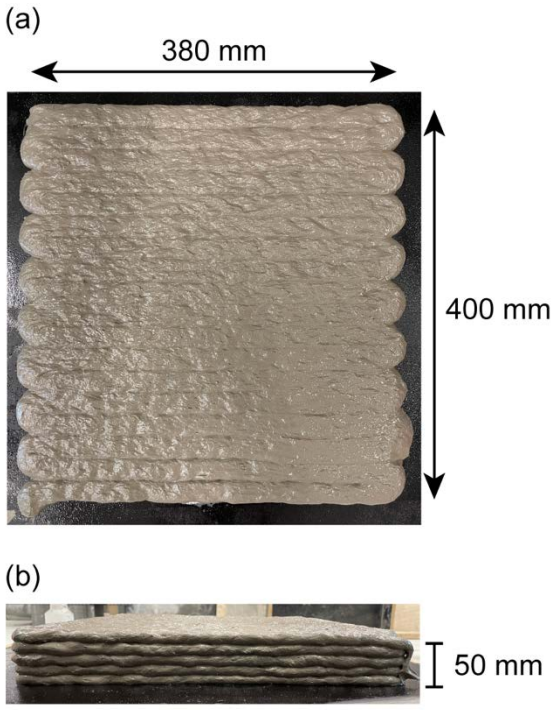

Figure 11. 3D-printed SHGC slab in fresh state: (a) Top view, and (b) Side view.

 doi:10.20944/preprints202203.0335.v1

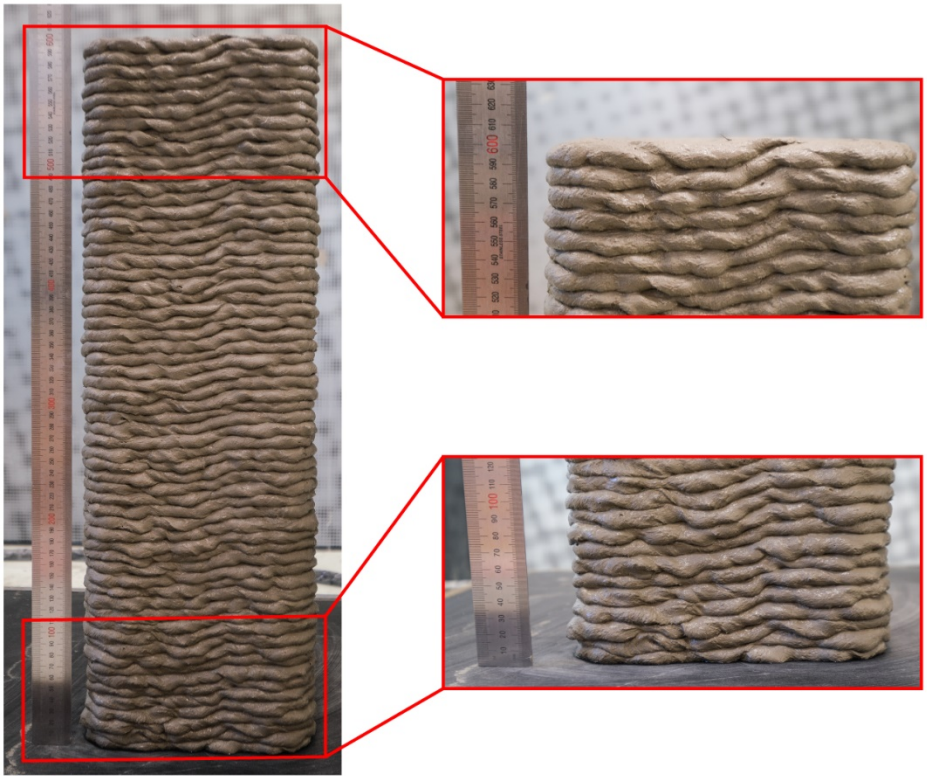

Figure 12. 3D-printed SHGC column in fresh state.

4.2.2. Workability and rheological properties

The average spread diameter of the 3DP-SHGC mixture was 161 mm after 25 strokes on the flow table, which is significantly smaller than that of the matrix (approximately 200 mm). Figure 13 shows the evolution of static yield stress of the 3DP-SHGC mixture. It should be noted that the self-protection mechanism of the rheometer was triggered as the measured torque value reached 5×10^3 N·mm. As indicated in the figure, the measured torque value exceeded 5×10^3 N·mm before the rest time of 10 min and thereby no readings were possible at 10 min and 15 min. The static yield stress of the fresh SHGC at each rest time was much higher than that of the matrix (i.e., FA50). This is mainly because of the lattice effect of the fibres [53], which increases the stress required to initiate the flow. Such high static yield stress values at each rest time explains the excellent shape-retention-ability and buildability of the SHGC mixture as observed in the buildability test.

Preprints (www.preprints.org) | NOT PEER-REVIEWED | Posted: 25 March 2022 doi:10.20944/preprints202203.0335.v1

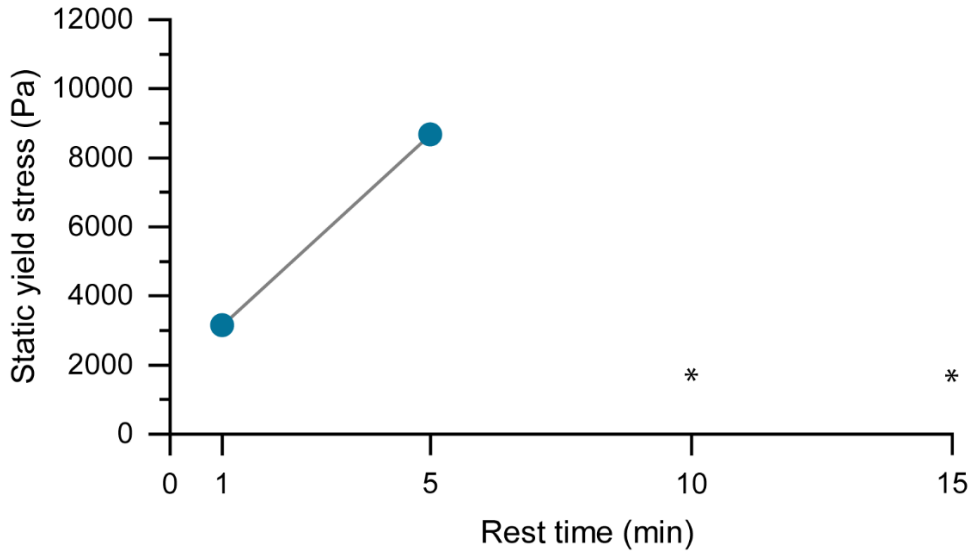

Figure 13. Static yield stress evolution of 3DP-SHGC. * No measurements were recorded for 10 min and 15 min resting times as the torque value exceeded 5×10^3 N·mm that triggered the self-protection mechanism of the rheometer.

Figure 14 presents the descending curve measured in the hysteresis test on the 3DP-SHGC mixture. According to the Reiner-Riwlin equation [54], the plastic viscosity and dynamic yield stress of the 3DP-SHGC mixture were 32.82 Pa·s and 145.63 Pa, respectively, which were higher than those of the matrix (i.e., FA50). The increase in the dynamic yield stress and plastic viscosity of the composite is most likely due to the already mentioned lattice effect of the PVA micro-fibres, which increases the stress needed to maintain the flow of the mixture. According to Chhabra and Richardson [55], the pumping pressure needed for conveying a Bingham fluid can be determined from Eq. (1):

$$P = \left(\frac{8\tau_d}{3R} + \frac{8\mu}{\pi R^4}Q\right)L \quad (1)$$

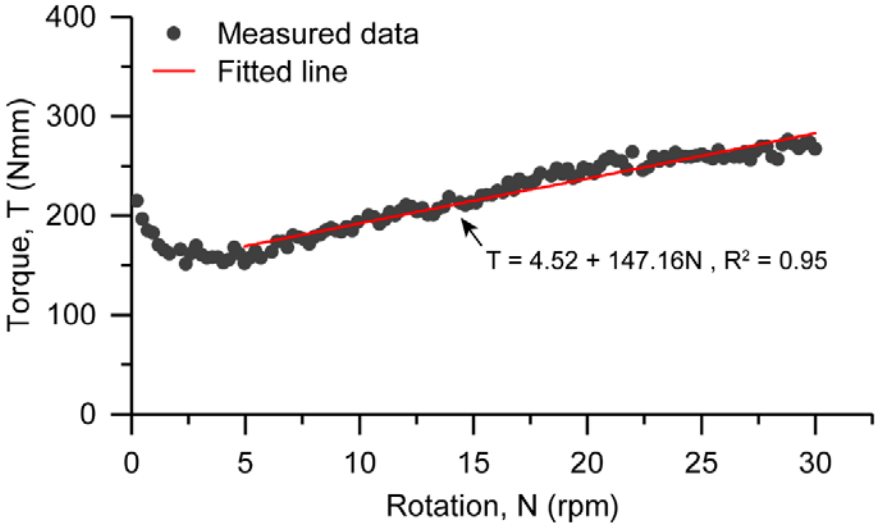

Figure 14. Descending curve of 3DP-SHGC measured in hysteresis test.

where τ_d and μ are dynamic yield stress (Pa) and plastic viscosity (Pa·s) of the material, respectively, Q is flow rate (m^3/s), P is pumping pressure (Pa), R and L are radius and length of hose (m), respectively. Using Eq. (1), the required pumping pressure for pumping the 3DP-SHGC mixture with the pump hose used in this paper (25 mm diameter

Preprints (www.preprints.org) | NOT PEER-REVIEWED | Posted: 25 March 2022 doi:10.20944/preprints202203.0335.v1

and 5 m length) at 0.75 L/min was determined to be 3.7 bar that is much lower when compared to the maximum capacity of the concrete pumping machine used in this paper (i.e., 20 bar). It should be noted here that more precise estimation of pumping pressure requires the definition of flow regime in the pipe (plug flow type or the shear flow type) and the rheological parameters of the lubricating layer forming at the pipe wall; see e.g. [56].

Figure 15 presents the apparent viscosity recovery. The fresh SHGC was only able to restore 29% of its initial apparent viscosity after 60 s from Stage II. This is despite the mixture contained nano clay, which is often used to improve the thixotropic of printable mixtures [22, 32, 57]. It is also interesting to point out that all matrices investigated in Section 4.1 were able to restore 89% to 94% of their initial apparent viscosity within 60 s after removing the constant high shear rate. To further investigate the thixotropic recovery of the SHGC mixture, its apparent viscosity at Stage III was measured for 330 s. As shown in Figure 15, the apparent viscosity of the mixture slowly recovered up to 62% of its initial apparent viscosity after 240 s (4 min) from Stage II. The reduction of the apparent viscosity recovery rate of the mixture in comparison to geopolymer mixtures without fibre is most likely due to the hydrophobic character of the oil coated PVA fibres used in this study. This hydrophobic character could cause the re-flocculation difficult to form on the surface of the fibres after shearing, and thereby reduce the apparent viscosity recovery rate of the mixture. Furthermore, it is likely that the presence of fibre enables a more uniform dispersion of fines in the mixture and consequently low tendency to agglomeration.

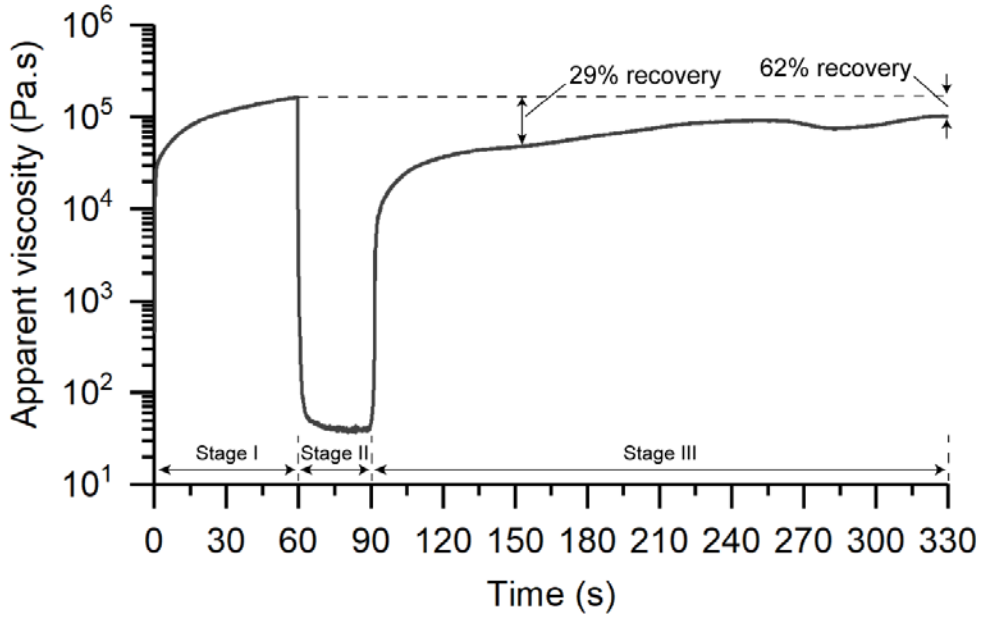

Figure 15. Apparent viscosity of 3DP-SHGC.

4.2.3. Mechanical properties

Figure 16 shows the compressive strength of one-part SHGC specimens with different curing temperatures and manufacturing processes. As expected, the compressive strength of the printed specimens was 6% to 25% lower than that of the mould-cast SHGC specimens, which depends on the loading direction and curing temperature. This result is in a good agreement with the compressive strength results for the 3D-printable OPC-based mortars reported in the literature [14, 58]. This tendency can be traced back to the higher porosity of the 3D-printed specimens as compared to that of the mould-cast specimens. The average density of mould-cast SHGC specimens cured at elevated temperature and ambient temperature were measured to be 1895 kg/m^3 and 1921 kg/m^3, respectively, which were higher than those of the 3D-printed specimens (1854

Preprints (www.preprints.org) | NOT PEER-REVIEWED | Posted: 25 March 2022 doi:10.20944/preprints202203.0335.v1

kg/m³ for heat curing and 1874 kg/m³ for ambient temperature curing). As shown in Figure 16, irrespective of the loading direction and manufacturing process, the strength of heat cured SHGC specimens was lower than that of the ambient temperature cured specimens. This result is in a good agreement with the compressive strength results of the one-part geopolymer matrices reported in Section 4.1 of this study.

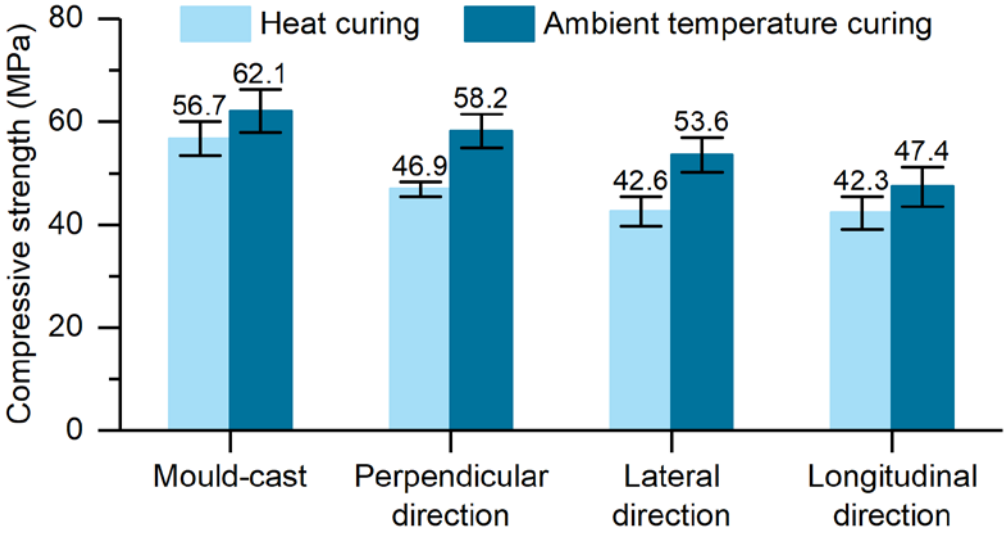

Figure 16. Compressive strength of mould-cast and 3D-printed SHGC.

For both curing regimes under investigation, the strength of 3D-printed SHGC specimens showed anisotropic property. The highest strength was measured in the perpendicular direction followed by those tested in the lateral direction and in the longitudinal direction. The compressive strengths of SHGC cured at ambient temperature in perpendicular, lateral and longitudinal directions were 24%, 25% and 12% higher than those of the heat cured SHGC, respectively. It is worth to point out that the same anisotropic pattern was also observed in the previous study of the authors [59] and the reasons for this pattern were described there.

Figure 17 shows the flexural stress vs. mid-span deflection curves of SHGC specimens produced using different curing temperatures and manufacturing processes. Irrespective of the curing temperature, both mould-cast and 3D-printed SHGC specimens showed deflection-hardening behaviour with numerous fine cracks when tested in bending. In addition, it is obvious that the flexural stress-deflection curves of 3D-printed specimens were higher and longer than those of the mould-cast specimens, indicating an improvement in flexural strength and deflection capacity due to the 3D printing process. This is true for both curing temperatures.

Preprints (www.preprints.org) | NOT PEER-REVIEWED | Posted: 25 March 2022 doi:10.20944/preprints202203.0335.v1

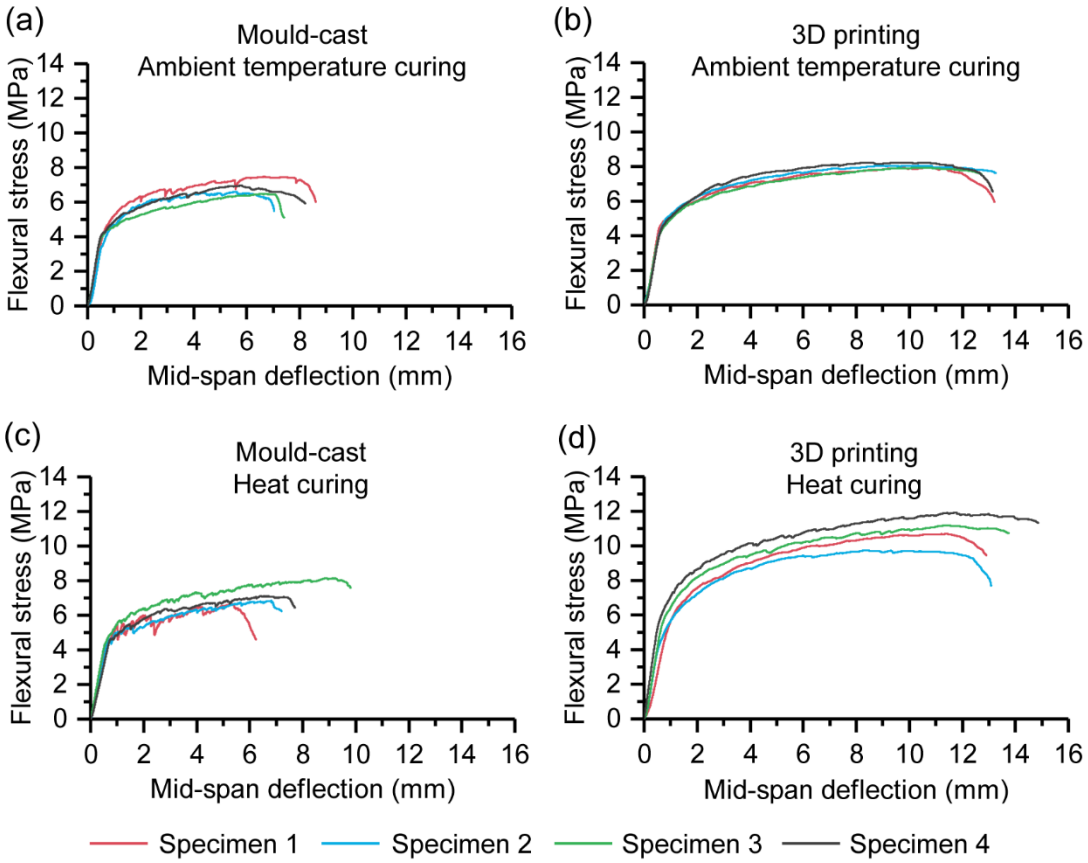

Figure 17. Flexural stress vs. mid-span deflection curves of SHGC specimens made with different curing temperatures and manufacturing processes.

Table 5 summarises the average first-crack strength f_{LOP}, modulus of rupture MOR and their corresponding deflection values (δ_{LOP} and δ_{MOR}, respectively) for SHGC specimens made with different curing temperatures and manufacturing processes. It can be seen that, regardless of the manufacturing process, all these parameters were higher for the heat cured specimens in comparison to those cured at ambient temperature. Based on the curing temperature, the average MOR and δ_{MOR} of 3D-printed specimens were 16% to 51% and 57% to 65% greater than those of the mould-cast SHGC specimens, respectively. This can be traced back to the fibre alignment in the 3D-printed specimens parallel to the direction of printing; see Figure 18. Such alignment of fibres perpendicular to cracks can significantly increase their crack bridging efficiency and thus result in higher MOR and δ_{MOR} values. In addition, a considerable number of fibre channels formed by fibre pullout were observed on the fracture surface, confirming a ductile failure mode. In contrast, the fibres were more randomly distributed in the mould-cast specimens, which led to their inferior deflection-hardening behaviour [60].

Preprints (www.preprints.org) | NOT PEER-REVIEWED | Posted: 25 March 2022 doi:10.20944/preprints202203.0335.v1

Table 5. Flexural test results for SHGC made with different manufacturing processes and curing temperatures.

Manufacturing process	Curing temperature	First-crack strength f_{LOP} (MPa)	First-crack deflection δ_{LOP} (mm)	Modulus of rupture MOR (MPa)	Deflection at peak load δ_{MOR} (mm)
Casting	Ambient	3.9 ± 0.3	0.5 ± 0.1	6.9 ± 0.4	6.2 ± 0.5
3D printing	Ambient	4.3 ± 0.1	0.6 ± 0.1	8.0 ± 0.1	10.2 ± 0.3
Casting	Heat	4.4 ± 0.1	0.7 ± 0.1	7.2 ± 0.6	6.9 ± 1.3
3D printing	Heat	5.3 ± 0.4	0.7 ± 0.2	10.9 ± 0.8	10.8 ± 1.4

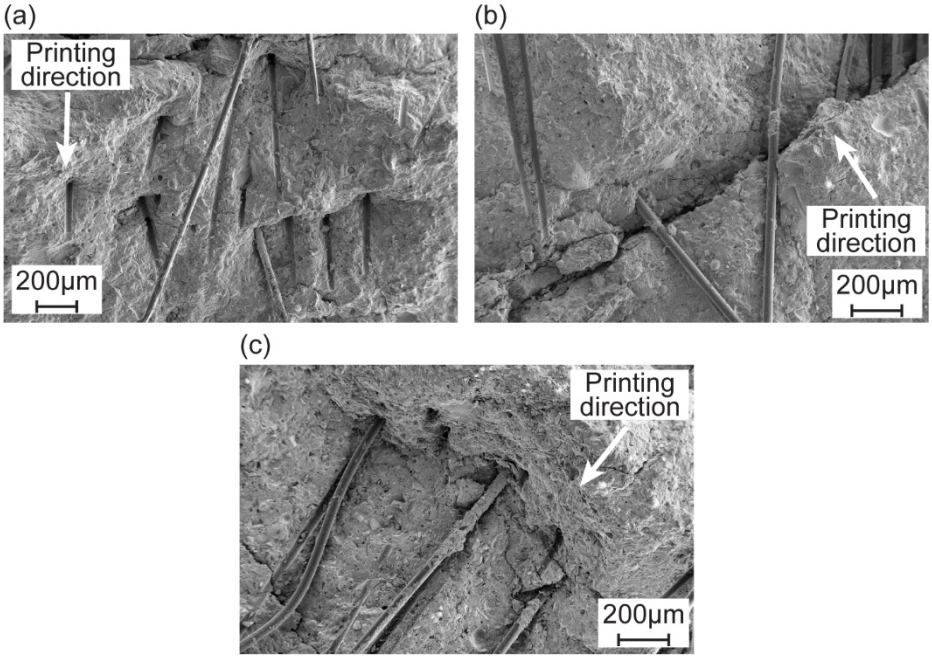

Figure 18. SEM images of the fracture surfaces of 3D-printed SHGC specimens.

The significant difference in the δ_{MOR} of mould-cast and 3D-printed SHGC specimens was also due to their different MOR/f_{LOP} ratios. Composite with higher MOR/f_{LOP} ratio has greater possibility to achieve better deflection-hardening behaviour, which leads to higher δ_{MOR} of the composite [61]. Based on Table 5, the MOR/f_{LOP} ratio of the 3D-printed specimens cured at ambient temperature and elevated temperature were 1.86 and 2.05, respectively, which were 5% to 25% higher than those obtained for the mould-cast specimens (1.77 for ambient temperature curing and 1.64 for heat curing).

Table 6 presents the ductility index and average work-to-fracture of SHGC specimens with different curing temperatures and manufacturing processes. The ductility of the SHGC specimens can be evaluated by the ductility index $\delta_{MOR}/\delta_{LOP}$ (i.e., the ratio of deflection at peak load to first crack deflection) defined by Naaman and Reinhardt [62]. The average work-to-fracture of the SHGC specimens was determined from the area under the flexural stress-deflection curves (Figure 17) up to the δ_{MOR}. As shown in the table, depending on the curing temperature, the ductility index of the 3D-printed SHGC specimens was 37% to 56% greater than that of the mould-cast SHGC specimens, which is because of the higher δ_{MOR} of the 3D-printed SHGC specimens. The average work-to-fracture of 3D-printed SHGC specimens was 106% to 138% higher than that of the mould-

Preprints (www.preprints.org) | NOT PEER-REVIEWED | Posted: 25 March 2022 doi:10.20944/preprints202203.0335.v1

cast specimens, based on the curing temperature. These results clearly indicate the significantly better flexural performance of the 3D-printed specimens to the mould-cast specimens. The ductility index of the specimens cured at ambient temperature was higher than that of the specimens cured at elevated temperature. However, the average work-to-fracture of the SHGC specimens cured at ambient temperature was lower than that of the counterpart heat cured SHGC specimens, which is due to the higher average f_{LOP}, MOR and their corresponding deflection values of the specimens subjected to heat curing. This holds true regardless of the manufacturing process.

Table 6. Ductility index and work-to-fracture of SHGC with different manufacturing processes and curing temperatures.

Manufacturing process	Curing temperature	Ductility index (-)	Work-to-fracture (kJ/m²)
Casting	Ambient	12.4	35.2 ± 4.1
3D printing	Ambient	17.0	72.4 ± 1.4
Casting	Heat	9.9	41.4 ± 11.8
3D printing	Heat	15.4	98.4 ± 19.0

Figure 19 presents the typical cracking patterns of mould-cast and 3D-printed SHGC specimens after unloading. Before making photographs, a small amount of water was sprayed on the specimen to obtain clear visible cracks as shown in the figure. The cracks' spacing observed on the mould-cast specimen was greater than that of the 3D-printed specimen. In addition, the number of cracks observed on the mould-cast specimen was significantly lower which corresponds to its lower deflection capacity compared to that of the 3D-printed specimens. On the contrary, saturated multiple fine cracks were observed over the mid-span of the 3D-printed specimen; see Figure 19b.

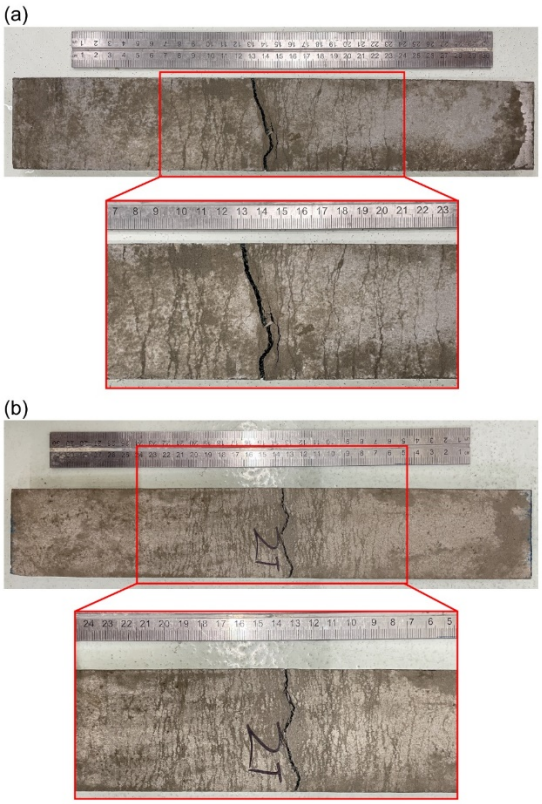

Figure 19. Cracking patterns of (a) mould-cast and (b) 3D-printed SHGC.

Preprints (www.preprints.org) | NOT PEER-REVIEWED | Posted: 25 March 2022 doi:10.20944/preprints202203.0335.v1

Figure 20 presents the tensile stress vs. strain curves for SHGC specimens made with different curing temperatures and manufacturing processes. As can be seen in Figure 20, regardless of the curing temperature, both mould-cast and 3D-printed SHGC specimens exhibited strain-hardening behaviour with multiple fine cracks under uniaxial tension. In addition, regardless of the manufacturing process, the tensile stress-strain curves of ambient temperature cured specimens indicated a higher strain capacity due to the heat curing.

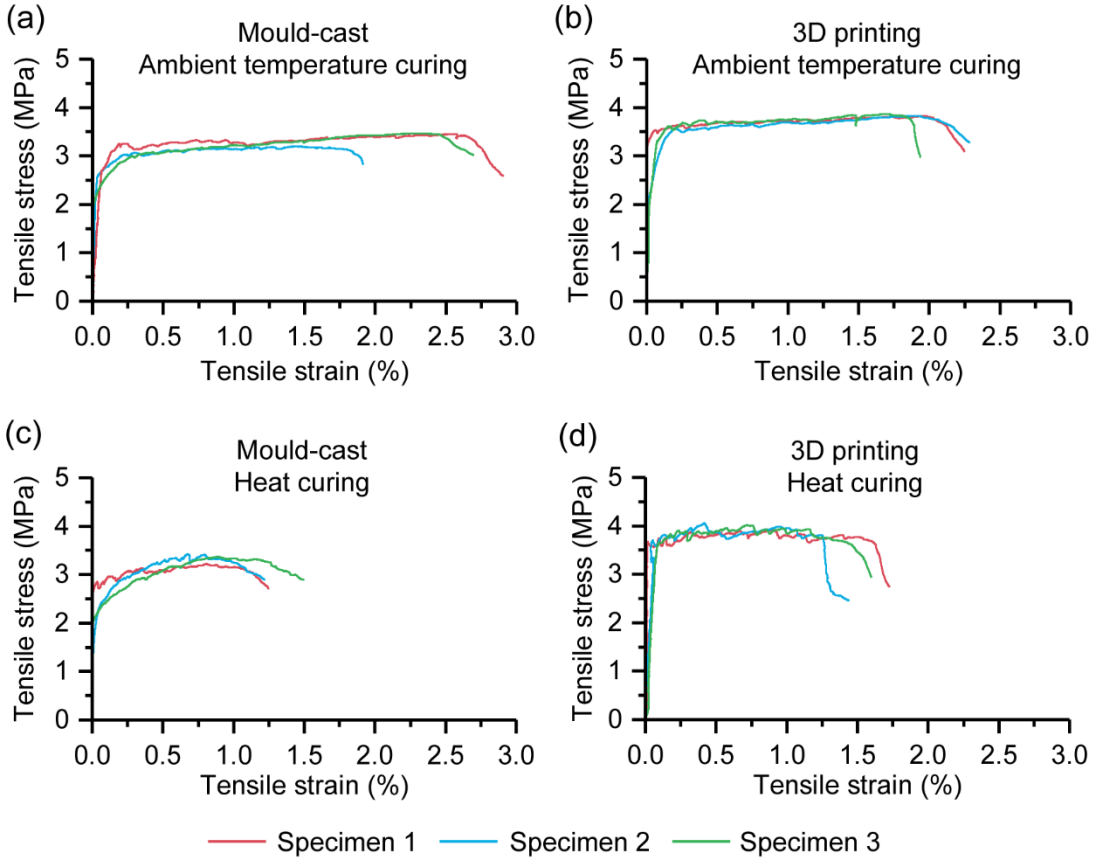

Figure 20. Tensile stress-strain curves of SHGC specimens made with different curing temperatures and manufacturing processes.

Table 7 summarises the average first-crack strength σ_{fc}, ultimate tensile strength σ_{ult}, tensile strain capacity ε_{ult} and work-to-fracture of SHGC specimens made with different curing temperatures and manufacturing processes. The last parameter was determined from the area under the tensile stress-strain curves (Figure 20) up to ε_{ult} corresponding to σ_{ult}. Table 7 shows that depending on the curing temperature, the average σ_{fc} and σ_{ult} of 3D-printed SHGC specimens were 26% to 48% and 12% to 21% higher than those of mould-cast SHGC specimens, respectively. In contrast to the random distribution of fibres in the mould-cast specimen, most fibres were aligned parallel to the direction of the applied tension force in the 3D-printed SHGC specimens, leading to the enhancement of the total crack-bridging capacity of the 3D-printed SHGC specimens. However, the average ε_{ult} of the mould-cast specimens was slightly higher than that of the 3D-printed SHGC specimens irrespective of the curing temperature. This can be due to more and larger voids formed in the 3D-printed SHGC specimens compared with the cast SHGC specimens; see Figure 21. Such voids are inevitably formed between layers and/or filaments during the 3D-printing process [63], despite cautious control of printing process and rheological properties of printing material [14]. In addition, the inclusion of short PVA fibres also increases the possibility of air entrapped in the mixture during the 3D printing process which results in more and larger air voids form in the 3D-printed

Preprints (www.preprints.org) | NOT PEER-REVIEWED | Posted: 25 March 2022 doi:10.20944/preprints202203.0335.v1

specimens. Lower strain capacity of 3D-printed ECC specimens has also been reported by Ye et al. [24, 25]. The average work-to-fracture of both mould-cast and 3D-printed specimens was comparable. This holds true regardless of the curing temperature.

Table 7. Uniaxial tension test results for SHGC made with different manufacturing processes and curing temperatures.

Manufacturing process	Curing temperature	First-crack strength σ_{fc} (MPa)	Ultimate tensile strength σ_{ult} (MPa)	Tensile strain capacity ε_{ult} (%)	Work-to-fracture (kJ/m^3)
Casting	Ambient	2.7 ± 0.1	3.4 ± 0.1	2.1 ± 0.5	67.9 ± 16.8
3D printing	Ambient	3.4 ± 0.1	3.8 ± 0.1	1.8 ± 0.1	67.1 ± 4.7
Casting	Heat	2.5 ± 0.2	3.3 ± 0.1	0.8 ± 0.1	23.6 ± 2.6
3D printing	Heat	3.7 ± 0.1	4.0 ± 0.1	0.7 ± 0.2	24.8 ± 7.6

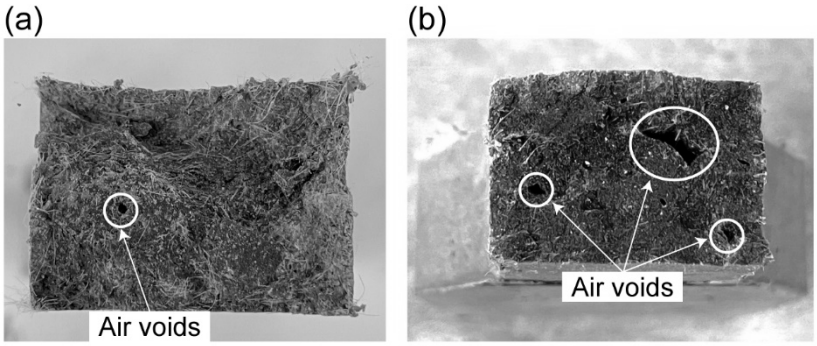

Figure 21. Fracture surface of (a) mould-cast and (b) 3D-printed SHGC specimens after failure in uniaxial tension test.

As can be seen in Table 7 for both manufacturing processes, the ε_{ult} and work-to-fracture of heat cured specimens were noticeably lower than those of the SHGC specimens cured at ambient temperature. This result is opposite to the flexural test results. Figure 22 presents the typical cracking patterns of mould-cast and 3D-printed SHGC specimens made with different curing temperatures. The number of cracks observed on the specimens cured at the ambient temperature after unloading was significantly higher in comparison to that of the counterpart specimens subjected to the heat curing. This is in agreement with the high ε_{ult} and work-to-fracture of the ambient temperature cured specimens. In addition, regardless of the curing temperature, the number of cracks observed on the 3D-printed specimens was significantly smaller than that of the mould-cast specimens, corresponding to the slightly lower ε_{ult} of the 3D-printed specimens. As both flexural and tensile performances of SHGC are closely related to the matrix fracture properties and fibre-matrix interface properties, further studies on micromechanics are required to clarify the reasons of various tendencies observed in flexural and uniaxial tension tests.

 doi:10.20944/preprints202203.0335.v1

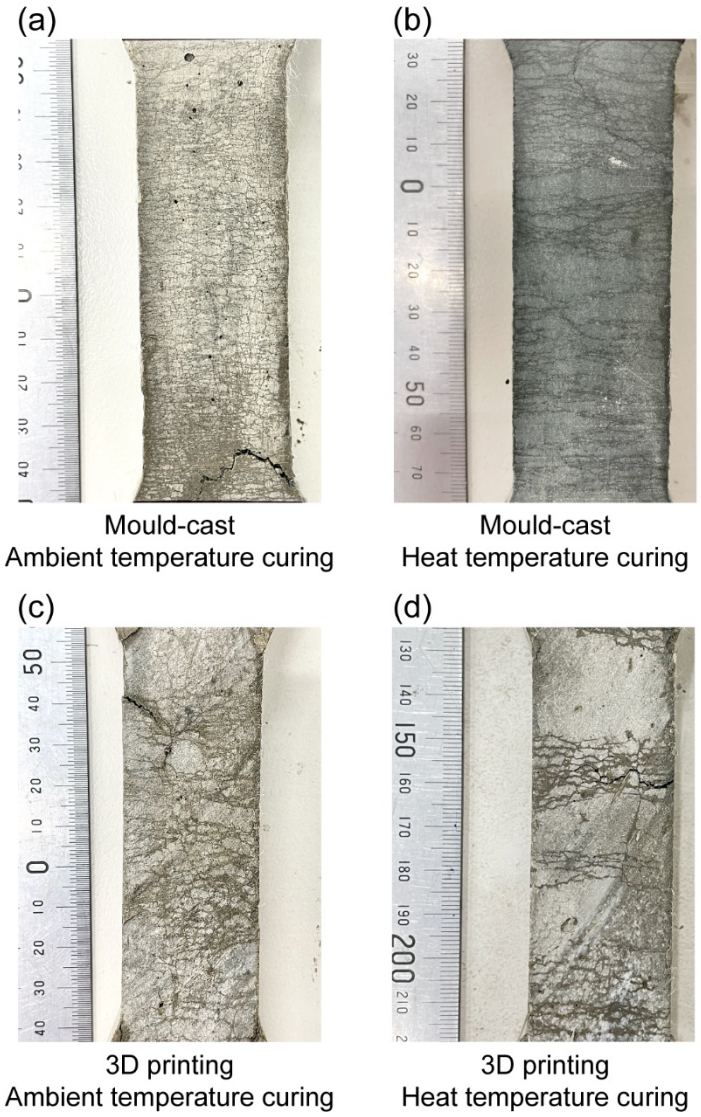

Figure 22. Cracking patterns of SHGC specimens with different curing temperatures and manufacturing processes.

5. Conclusions

This paper focused on formulating a 3D-printable strain-hardening geopolymer composite (3D-SHGC) exhibiting quasi-ductile behaviour in direct tension. First, the matrix was optimised by investigating the influence of FA to GGBFS mass ratio on the rheological properties and compressive strength of geopolymer matrices. The compressive strength of the geopolymer matrices cured at different temperatures was also measured. The printing performance and rheological properties of the developed 3DP-SHGC with the optimum matrix were then evaluated. The mechanical properties (under compression, bending and tension) of the 3D-printed and mould-cast SHGCs were measured. The following conclusions can be drawn:

(1) The static yield stress, plastic viscosity and dynamic yield stress of the one-part geopolymer matrix increased as the FA to GGBFS ratio increased.

(2) The one-part geopolymer matrices cured at ambient temperature exhibited higher compressive strength than that of the heat cured specimens. Among the matrices investigated in this study, FA50 with the fly ash to slag ratio of 1.0 showed the highest compressive strength of 58.6 to 66.0 MPa depending on the curing temperature.

(3) The developed 3DP-SHGC mixture exhibited adequate extrudability and excellent buildability which was corroborated by the rapid evolution of static yield stress of the fresh material.
(4) The thixotropic recovery of SHGC was significantly reduced which is likely due to the hydrophobic character of the oil coated PVA fibres used in this study.
(5) The compressive strength of the 3D-printed SHGC was in the range 42.3 to 58.2 MPa, based on the loading direction and temperature of curing. The 3D-printed SHGC showed 6% to 25% lower compressive strength than that of the mould-cast SHGC, based on the loading direction and temperature of curing.
(6) The compressive strengths of 3D-printed ambient temperature cured SHGC in perpendicular, lateral and longitudinal directions were 24%, 25% and 12% higher than those of the 3D-printed heat cured SHGC, respectively.
(7) Both the mould-cast and 3D-printed SHGC showed deflection-hardening behaviour with numerous fine cracks when tested in bending irrespective of the curing temperature. The f_{LOP}, MOR and their corresponding deflection values of the 3D-printed SHGC were significantly higher than those of the mould-cast SHGC. Moreover, the heat cured SHGC exhibited higher f_{LOP}, MOR and their corresponding deflection values than those of the counterpart SHGC cured at ambient temperature.
(8) Both mould-cast and 3D-printed SHGC exhibited strain-hardening behaviour with numerous fine cracks under uniaxial tension. This holds true irrespective of curing temperature. The σ_{fc} and σ_{ult} of 3D-printed SHGC were 26% to 48% and 12% to 21% higher than those of mould-cast SHGC, respectively. However, the ε_{ult} of the mould-cast SHGC was slightly higher than that of the 3D-printed SHGC due to large air voids formed in the 3D-printed SHGC. Furthermore, regardless of the manufacturing process, the tensile strain capacity of heat cured specimens (0.7% to 0.8%) was notably lower than that of the SHGC cured at ambient temperature (1.8% to 2.1%).

Acknowledgments: This project was supported by the Discovery Project DP210101680, Discovery Early Career Researcher Award DE180101587 and Linkage Infrastructure Grant LE170100168, funded by the Australian Research Council, as well as the 2018 Australia–Germany Joint Research Co-operation Scheme grant funded by Universities Australia and German Academic Exchange Service.

References

[1] F. Barbosa, J. Woetzel, J. Mischke, M. J Ribeirinho, M. Sridhar, M. Parsons, N. Bertram, S. Brown, Reinventing construction: a route to higher productivity, McKinsey Global Institute, 2017.
[2] J.G. Sanjayan, B. Nematollahi, 3D concrete printing for construction applications, 3D Concrete Printing Technology, Elsevier2019, pp. 1-11.
[3] B. Khoshnevis, Automated construction by contour crafting—related robotics and information technologies, Autom. Constr. 13(1) (2004) 5-19.
[4] S.C. Paul, G.P. van Zijl, M.J. Tan, I. Gibson, A review of 3D concrete printing systems and materials properties: Current status and future research prospects, Rapid Prototyp. J. 24(4) (2018) 784-798.
[5] V. Mechtcherine, R. Buswell, H. Kloft, F.P. Bos, N. Hack, R. Wolfs, J. Sanjayan, B. Nematollahi, E. Ivaniuk, T. Neef, Integrating reinforcement in digital fabrication with concrete: A review and classification framework, Cement Concr. Compos. 119 (2021) 103964.
[6] P. Wu, J. Wang, X. Wang, A critical review of the use of 3-D printing in the construction industry, Autom. Constr. 68 (2016) 21-31.
[7] T.A.M. Salet, Z.Y. Ahmed, F.P. Bos, H.L.M. Laagland, Design of a 3D printed concrete bridge by testing, Virtual Phys. Prototyp. 13(3) (2018) 222-236.
[8] T. Marchment, J. Sanjayan, Mesh reinforcing method for 3D Concrete Printing, Autom. Constr. 109 (2020) 102992.
[9] J.H. Lim, B. Panda, Q.-C. Pham, Improving flexural characteristics of 3D printed geopolymer composites with in-process steel cable reinforcement, Construct. Build. Mater. 178 (2018) 32-41.

[10] F.P. Bos, Z.Y. Ahmed, E.R. Jutinov, T.A. Salet, Experimental exploration of metal cable as reinforcement in 3D printed concrete, Materials 10(11) (2017) 1314.
[11] V. Mechtcherine, A. Michel, M. Liebscher, T. Schmeier, Extrusion-based additive manufacturing with carbon reinforced concrete: Concept and feasibility study, Materials 13(11) (2020).
[12] A.R. Arunothayan, B. Nematollahi, R. Ranade, S.H. Bong, J. Sanjayan, Development of 3D-printable ultra-high performance fiber-reinforced concrete for digital construction, Construct. Build. Mater. 257 (2020) 119546.
[13] B. Panda, S.C. Paul, M.J. Tan, Anisotropic mechanical performance of 3D printed fiber reinforced sustainable construction material, Mater. Lett. 209 (2017) 146-149.
[14] T.T. Le, S.A. Austin, S. Lim, R.A. Buswell, R. Law, A.G. Gibb, T. Thorpe, Hardened properties of high-performance printing concrete, Cement Concr. Res. 42(3) (2012) 558-566.
[15] V.C. Li, F.P. Bos, K. Yu, W. McGee, T.Y. Ng, S.C. Figueiredo, K. Nefs, V. Mechtcherine, V.N. Nerella, J. Pan, G.P.A.G. van Zijl, P.J. Kruger, On the emergence of 3D printable Engineered, Strain Hardening Cementitious Composites (ECC/SHCC), Cement Concr. Res. 132 (2020) 106038.
[16] T. Matsumoto, H. Mihashi, DFRCC terminology and application concepts, J. Adv. Concr. Technol. 1(3) (2003) 335-340.
[17] B. Nematollahi, J. Sanjayan, F.U.A. Shaikh, Matrix design of strain hardening fiber reinforced engineered geopolymer composite, Compos. B. Eng. 89 (2016) 253-265.
[18] V.C. Li, On engineered cementitious composites (ECC) a review of the material and its applications, J. Adv. Concr. Technol. 1(3) (2003) 215-230.
[19] K. Yu, L. Li, J. Yu, J. Xiao, J. Ye, Y. Wang, Feasibility of using ultra-high ductility cementitious composites for concrete structures without steel rebar, Eng. Struct. 170 (2018) 11-20.
[20] H. Ogura, V.N. Nerella, V. Mechtcherine, Developing and testing of strain-hardening cement-based composites (SHCC) in the context of 3D-printing, Materials 11(8) (2018) 1375.
[21] D.G. Soltan, V.C. Li, A self-reinforced cementitious composite for building-scale 3D printing, Cement Concr. Compos. 90 (2018) 1-13.
[22] B. Zhu, J. Pan, B. Nematollahi, Z. Zhou, Y. Zhang, J. Sanjayan, Development of 3D printable engineered cementitious composites with ultra-high tensile ductility for digital construction, Mater. Des. 181 (2019) 108088.
[23] S. Chaves Figueiredo, C. Romero Rodríguez, Z.Y. Ahmed, D.H. Bos, Y. Xu, T.M. Salet, O. Çopuroğlu, E. Schlangen, F.P. Bos, An approach to develop printable strain hardening cementitious composites, Mater. Des. 169 (2019) 107651.
[24] J. Ye, C. Cui, J. Yu, K. Yu, F. Dong, Effect of polyethylene fiber content on workability and mechanical-anisotropic properties of 3D printed ultra-high ductile concrete, Construct. Build. Mater. 281 (2021) 122586.
[25] J. Ye, C. Cui, J. Yu, K. Yu, J. Xiao, Fresh and anisotropic-mechanical properties of 3D printable ultra-high ductile concrete with crumb rubber, Compos. B. Eng. 211 (2021) 108639.
[26] D.N. Huntzinger, T.D. Eatmon, A life-cycle assessment of portland cement manufacturing: comparing the traditional process with alternative technologies, J. Clean. Prod. 17(7) (2009) 668-675.
[27] M. Taylor, C. Tam, D. Gielen, Energy efficiency and CO2 emissions from the global cement industry, Korea 50(2.2) (2006) 61-67.
[28] P. Nath, P.K. Sarker, Effect of GGBFS on setting, workability and early strength properties of fly ash geopolymer concrete cured in ambient condition, Construct. Build. Mater. 66 (2014) 163-171.
[29] P.S. Deb, P. Nath, P.K. Sarker, The effects of ground granulated blast-furnace slag blending with fly ash and activator content on the workability and strength properties of geopolymer concrete cured at ambient temperature, Mater. Des. 62 (2014) 32-39.
[30] ASTM C1437-15, Standard test method for flow of hydraulic cement mortar, ASTM International, West Conshohocken, PA USA.
[31] E.-H. Yang, M. Sahmaran, Y. Yang, V.C. Li, Rheological control in production of engineered cementitious composites, ACI Mater. J. 106(4) (2009) 357.
[32] B. Panda, S. Ruan, C. Unluer, M.J. Tan, Improving the 3D printability of high volume fly ash mixtures via the use of nano attapulgite clay, Compos. B. Eng. 165 (2019) 75-83.
[33] Viskomat XL – rheometer for mortar and fresh concrete, (2020). http://www.schleibinger.com/cmsimple/en/?Rheometers:Viskomat_XL_-_Rheometer_for_Mortar_and_Fresh_Concrete (accessed April 20, 2021).
[34] V.N. Nerella, M.A.B. Beigh, S. Fataei, V. Mechtcherine, Strain-based approach for measuring structural build-up of cement pastes in the context of digital construction, Cement Concr. Res. 115 (2019) 530-544.
[35] I. Ivanova, V. Mechtcherine, Evaluation of structural build-up rate of cementitious materials by means of constant shear rate test: Parameter study, RILEM Bookseries, 2020, pp. 209-218.
[36] S. Muthukrishnan, S. Ramakrishnan, J. Sanjayan, Effect of alkali reactions on the rheology of one-part 3D printable geopolymer concrete, Cement Concr. Compos. 116 (2021) 103899.
[37] L.E. Malvern, Introduction to the mechanics of a continuous medium, Prentice-Hall, Englewood Cliffs, N.J., 1969.
[38] S.H. Bong, M. Xia, B. Nematollahi, C. Shi, Ambient temperature cured 'just-add-water' geopolymer for 3D concrete printing applications, Cement Concr. Compos. (2021) 104060.
[39] H. Li, Y.J. Tan, K.F. Leong, L. Li, 3D bioprinting of highly thixotropic alginate/methylcellulose hydrogel with strong interface bonding, ACS Appl. Mater. Interfaces 9(23) (2017) 20086-20097.
[40] S.H. Bong, B. Nematollahi, A.R. Arunothayan, M. Xia, J. Sanjayan, Effect of wollastonite micro-fiber addition on properties of 3D-printable 'just-add-water' geopolymers, RILEM Bookseries, 2020, pp. 23-31.

 doi:10.20944/preprints202203.0335.v1

[41] N. Roussel, Rheological requirements for printable concretes, Cement Concr. Res. 112 (2018) 76-85.
[42] Q. Yuan, Z. Li, D. Zhou, T. Huang, H. Huang, D. Jiao, C. Shi, A feasible method for measuring the buildability of fresh 3D printing mortar, Construct. Build. Mater. 227 (2019) 116600.
[43] W.-C. Wang, H.-Y. Wang, M.-H. Lo, The fresh and engineering properties of alkali activated slag as a function of fly ash replacement and alkali concentration, Construct. Build. Mater. 84 (2015) 224-229.
[44] C. Tennakoon, R. San Nicolas, J.G. Sanjayan, A. Shayan, Thermal effects of activators on the setting time and rate of workability loss of geopolymers, Ceram. Int. 42(16) (2016) 19257-19268.
[45] M. Chen, B. Liu, L. Li, L. Cao, Y. Huang, S. Wang, P. Zhao, L. Lu, X. Cheng, Rheological parameters, thixotropy and creep of 3D-printed calcium sulfoaluminate cement composites modified by bentonite, Compos. B. Eng. 186 (2020) 107821.
[46] P. Duxson, A. Fernández-Jiménez, J.L. Provis, G.C. Lukey, A. Palomo, J.S. van Deventer, Geopolymer technology: the current state of the art, J. Mater. Sci. 42(9) (2007) 2917-2933.
[47] Y. Weng, M. Li, M.J. Tan, S. Qian, Design 3D printing cementitious materials via Fuller Thompson theory and Marson-Percy model, Construct. Build. Mater. 163 (2018) 600-610.
[48] I. Ismail, S.A. Bernal, J.L. Provis, R. San Nicolas, S. Hamdan, J.S.J. van Deventer, Modification of phase evolution in alkali-activated blast furnace slag by the incorporation of fly ash, Cement Concr. Compos. 45 (2014) 125-135.
[49] M. Li, V.C. Li, Rheology, fiber dispersion, and robust properties of engineered cementitious composites, Mater. Struct. 46(3) (2013) 405-420.
[50] T.T. Le, S.A. Austin, S. Lim, R.A. Buswell, A.G. Gibb, T. Thorpe, Mix design and fresh properties for high-performance printing concrete, Mater. Struct. 45(8) (2012) 1221-1232.
[51] T. Ding, J. Xiao, S. Zou, Y. Wang, Hardened properties of layered 3D printed concrete with recycled sand, Cement Concr. Compos. 113 (2020) 103724.
[52] W. McGee, T.Y. Ng, K. Yu, V.C. Li, Extrusion nozzle shaping for improved 3DP of engineered cementitious composites (ECC/SHCC), Springer International Publishing, Cham, 2020, pp. 916-925.
[53] K.H. Khayat, W. Meng, K. Vallurupalli, L. Teng, Rheological properties of ultra-high-performance concrete—An overview, Cement Concr. Res. 124 (2019) 105828.
[54] M. Reiner, Deformation and flow: An elementary introduction to theoretical rheology, HK Lewis 1949.
[55] R.P. Chhabra, J.F. Richardson, Non-Newtonian flow and applied rheology: engineering applications, Butterworth-Heinemann, 2011.
[56] E. Secrieru, W. Mohamed, S. Fataei, V. Mechtcherine, Assessment and prediction of concrete flow and pumping pressure in pipeline, Cement Concr. Compos. 107 (2020) 103495.
[57] B. Panda, S. Ruan, C. Unluer, M.J. Tan, Investigation of the properties of alkali-activated slag mixes involving the use of nanoclay and nucleation seeds for 3D printing, Compos. B. Eng. 186 (2020) 107826.
[58] R. Wolfs, F. Bos, T. Salet, Hardened properties of 3D printed concrete: The influence of process parameters on interlayer adhesion, Cement Concr. Res. 119 (2019) 132-140.
[59] S.H. Bong, B. Nematollahi, M. Xia, A. Nazari, J. Sanjayan, J. Pan, Properties of 3D-printable ductile fibre-reinforced geopolymer composite for digital construction applications, RILEM Bookseries, 2020, pp. 363-372.
[60] A.R. Arunothayan, B. Nematollahi, R. Ranade, S.H. Bong, J.G. Sanjayan, K.H. Khayat, Fiber orientation effects on ultra-high performance concrete formed by 3D printing, Cement Concr. Res. 143 (2021) 106384.
[61] T. Kanda, V.C. Li, Practical design criteria for saturated pseudo strain hardening behavior in ECC, J. Adv. Concr. Technol. 4(1) (2006) 59-72.
[62] A. Naaman, H. Reinhardt, Characterization of high performance fiber reinforced cement composites, High performance fiber reinforced cement composites—HPFRCC, 1996, pp. 1-24.
[63] G. Ma, J. Zhang, L. Wang, Z. Li, J. Sun, Mechanical characterization of 3D-printed anisotropic cementitious material by the electromechanical transducer, Smart Mater Struct. 27(7) (2018) 075036.